Monthly Notices of the ROYAL ASTRONOMICAL SOCIETY

MNRAS **518,** 5522–5535 (2023) https://doi.org/10.1093/mnras/stac3451
Advance Access publication 2022 November 25

Predicting sub-millimetre flux densities from global galaxy properties

R. K. Cochrane [1,2]★ C. C. Hayward [1] D. Anglés-Alcázar [1,3] and R. S. Somerville [1]

[1]*Center for Computational Astrophysics, Flatiron Institute, 162 Fifth Avenue, New York, NY 10010, USA*
[2]*Harvard–Smithsonian Center for Astrophysics, 60 Garden Street, Cambridge, MA 02138, USA*
[3]*Department of Physics, University of Connecticut, 196 Auditorium Road, U-3046, Storrs, CT 06269-3046, USA*

Accepted 2022 November 22. Received 2022 November 10; in original form 2022 August 29

ABSTRACT

Recent years have seen growing interest in post-processing cosmological simulations with radiative transfer codes to predict observable fluxes for simulated galaxies. However, this can be slow, and requires a number of assumptions in cases where simulations do not resolve the interstellar medium (ISM). Zoom-in simulations better resolve the detailed structure of the ISM and the geometry of stars and gas; however, statistics are limited due to the computational cost of simulating even a single halo. In this paper, we make use of a set of high-resolution, cosmological zoom-in simulations of massive ($M_\star \gtrsim 10^{10.5}\,\mathrm{M}_\odot$ at $z = 2$), star-forming galaxies from the FIRE suite. We run the SKIRT radiative transfer code on hundreds of snapshots in the redshift range $1.5 < z < 5$ and calibrate a power-law scaling relation between dust mass, star formation rate, and 870 μm flux density. The derived scaling relation shows encouraging consistency with observational results from the sub-millimetre-selected AS2UDS sample. We extend this to other wavelengths, deriving scaling relations between dust mass, stellar mass, star formation rate, and redshift and sub-millimetre flux density at observed-frame wavelengths between ∼340 and ∼870 μm. We then apply the scaling relations to galaxies drawn from EAGLE, a large box cosmological simulation. We show that the scaling relations predict EAGLE sub-millimetre number counts that agree well with previous results that were derived using far more computationally expensive radiative transfer techniques. Our scaling relations can be applied to other simulations and semi-analytical or semi-empirical models to generate robust and fast predictions for sub-millimetre number counts.

Key words: radiative transfer – galaxies: evolution – galaxies: starburst – galaxies: star formation – infrared: galaxies – submillimetre: galaxies.

1 INTRODUCTION

Robust constraints on the history of star formation in the Universe are fundamental to studies of galaxy evolution. Rest-frame ultraviolet (UV) surveys, particularly in the Hubble Deep Fields, have measured unobscured star formation out to $z \sim 9$ and beyond (e.g. Oesch et al. 2018; Bouwens et al. 2019, 2021, 2022; Stefanon et al. 2021; Finkelstein et al. 2022; Tacchella et al. 2022). However, such surveys are biased towards the least dust-obscured systems, which may represent a sub-dominant population at certain cosmic epochs. The population of rare but bright sub-millimetre galaxies (SMGs; Smail, Ivison & Blain 1997; Barger et al. 1998; Hughes et al. 1998; Blain et al. 2002) discovered by early single-dish sub-millimetre observations appears to contribute significantly to the star formation rate density of the Universe (SFRD). Zavala et al. (2021) estimate that dust-obscured star formation dominates the SFRD out to $z \sim 4$, and roughly equals the contribution of unobscured star formation (traced by the rest-frame UV and optical emission) at $z \sim 4$–5 (see also Swinbank et al. 2014; Dunlop et al. 2017; Casey et al. 2018; Bouwens et al. 2020).

The most extreme SMGs ($L_{\mathrm{IR}} \sim 10^{13}\,\mathrm{L}_\odot$) form stars at rates of thousands of solar masses per year, have established high stellar masses ($M_\star \sim 10^{11}\,\mathrm{M}_\odot$; Magnelli et al. 2012; Simpson et al. 2014; Da Cunha et al. 2015; Miettinen et al. 2017; Dudzeviciute et al. 2020) within the first few Gyr of cosmic time, and reside in the most massive haloes (Hickox et al. 2012; Wilkinson et al. 2017; Marrone et al. 2018; Miller et al. 2018; Garcia-Vergara et al. 2020; Stach et al. 2021). They hence place important constraints on the formation of dust and metals in the early Universe (Rowlands et al. 2014; Magnelli et al. 2020). However, detailed study of these systems has historically been difficult, due in part to the poor spatial resolution of single-dish telescopes such as SCUBA and the lack of deep multiwavelength data for cross-matching sub-millimetre detections (often of blended sources) to counterparts at other wavelengths.

However, recent developments in sub-millimetre interferometry, most recently the depth and angular resolution brought by ALMA, have transformed our understanding of SMGs (see the comprehensive review by Hodge & da Cunha 2020). We can now locate individual sources precisely, and derive much stronger constraints on source multiplicity (e.g. Stach et al. 2018 find that 28 ± 2 per cent of single-dish sources with $S_{850} \geq 5$ mJy are blends of two or more ALMA-detectable SMGs, each with flux density ≥ 1 mJy; see also Hayward et al. 2013a, b, 2018). This has led to more robust SMG number counts, redshift distributions, and counterpart identification, which has enabled estimates of physical properties (e.g. Dudzeviciute et al. 2020). We can now resolve the dust continuum and line emission of distant galaxies on sub-kiloparsec scales (and even lower for some

★ E-mail: rcochrane@flatironinstitute.org

strongly lensed sources; e.g. Rybak et al. 2015a, b, 2020; Fujimoto et al. 2021). A number of studies have reported that observed dust continuum emission is not co-located with emission in the rest-frame UV and optical (e.g. Chen et al. 2017; Cochrane et al. 2021), with the longer-wavelength emission typically being more compact (e.g. 1–2 kpc; Hodge et al. 2016; Tadaki et al. 2017; Calistro Rivera et al. 2018; Chen et al. 2020). In some high-redshift sources, dust attenuation is high enough to render the sources near-infrared-faint (see Smail et al. 2021, for a statistical study).

Despite these major observational strides, SMGs present a challenge to models of galaxy formation. The majority of semi-analytical models (SAMs) fail to match the number counts of SMGs, underpredicting their numbers by one to two orders of magnitude (e.g. Cole et al. 2000; Granato et al. 2000; Somerville et al. 2012). Previously explored solutions have involved invoking different variants of a top-heavy initial mass function (IMF; Baugh et al. 2005; Lacey et al. 2016; Cowley et al. 2019); adopting a particularly extreme flat IMF in starbursts enabled Baugh et al. (2005) to match observed SMG number counts and redshift distribution as well as the local *K*-band luminosity function. However, given the wide range of tuneable parameters in SAMs, it remains unclear whether this is the solution (Safarzadeh, Hayward & Ferguson 2017). One fundamental limitation is the lack of geometrical information in SAMs; while galaxies can be parametrized by, for example, a disc plus bulge component on which post-processing may be applied, the detailed relative geometries of dust and stars are not captured.

Hydrodynamical simulations track the positions of stellar and gas (and sometimes dust) particles, and hence do contain some information about their relative spatial distributions. There has been substantial recent interest in casting these simulations into the 'observational plane', made possible by radiative transfer codes such as SKIRT (Baes et al. 2011; Camps & Baes 2015), POWDERDAY (Narayanan et al. 2021), and SUNRISE (Jonsson, Groves & Cox 2010). These codes work by propagating photons from ionizing sources through a dust grid. Following substantial success in applying these codes to individual galaxies and limited samples of zoom-in simulations (e.g. Narayanan et al. 2010, 2015; Hayward et al. 2011, 2012; Cochrane et al. 2019; Parsotan et al. 2021; Cochrane, Hayward & Angles-Alcazar 2022), recent work has focused on application to large-scale cosmological simulations. The EAGLE project presents predictions for galaxy spectral energy distributions (SEDs) using SKIRT (Camps et al. 2016; Trayford et al. 2017). McAlpine et al. (2019) show the good agreement between the physical properties [including the redshift distribution, star formation rates (SFRs), and stellar and dust masses] of modelled and observed sub-millimetre sources (defined as those with $S_{850} \geq 1$ mJy). However, the number counts of the most extreme sources are at least an order of magnitude lower than inferred from observations (Cowley et al. 2019; Wang et al. 2019). Radiative transfer calculations (with POWDERDAY) have also been performed on the SIMBA simulations (Davé et al. 2019). Lovell et al. (2021) show that their model is more successful at matching observed 850 μm number counts than EAGLE (though the redshift distribution of bright > 3.6 mJy sources is skewed to higher redshifts than is currently measured by observations). SIMBA's larger number of sub-millimetre bright sources is tied to the 'on-the-fly' dust model, which produces galaxies with dust masses that are higher by a factor of ∼2.5 than those calculated using a more commonly adopted dust-to-metals ratio of 0.3 dex. It is also related to the distribution of SFRs at different redshifts: SIMBA models more high mass, high specific star formation rate galaxies than EAGLE at $z \sim 2$ and by $z > 4$ the global star formation rate density is higher than inferred from observations (Davé et al. 2019). These existing works highlight the utility of SMG number counts as one of numerous observational constraints for the various physical processes included in galaxy formation models, such as active galactic nucleus (AGN) and stellar feedback and dust physics.

One key limitation of applying radiative transfer to cosmological simulations is the computational resources required. For a project such as CAMELS (Villaescusa-Navarro et al. 2021, 2022), which involves thousands of simulations with different initial conditions and parameter choices, this is intractable. Furthermore, for large-box simulations like EAGLE, the resolution is low and particle mass is high ($\sim 10^6$ M$_\odot$), such that the cold molecular gas phase of the interstellar medium (ISM) is not resolved, and young stars can appear 'clumped' into a few, point-like regions (Camps et al. 2016). It is therefore necessary to artificially increase the particle mass and time resolution by performing a resampling procedure on the gas and young star particles prior to the radiative transfer procedure.

An alternative to running radiative transfer on large cosmological simulations is to apply well-calibrated scaling relations to the physical properties of simulated galaxies to estimate their fluxes. Hayward et al. (2011) used hydrodynamic simulations of isolated and merging galaxies to derive a relation between dust mass, SFR, and S_{850} (see also Hayward et al. 2013a). While a parametrized relation would be harder to derive for emission at shorter wavelengths, which have more complex dependencies on stellar populations and geometry/inclination, this works fairly well for sub-millimetre fluxes, which are expected to depend fundamentally on dust mass and dust temperature. Such a relation can then be applied to cosmological simulations (with lower particle resolution) to predict sub-millimetre flux densities with a trivial computational cost. Hayward et al. (2021) applied the scaling relation derived in Hayward et al. (2013a) to derive SMG number counts for galaxies in the original Illustris (Genel et al. 2014; Vogelsberger et al. 2014) and more recent IllustrisTNG simulations (Weinberger et al. 2017; Pillepich et al. 2018). Their predicted number counts for the two simulations differed significantly, with IllustrisTNG hosting fewer SMGs than Illustris by an order of magnitude. They argued that this was due to the lower dust masses and SFRs of high-mass galaxies in IllustrisTNG. These differences in demographics relate to the differing subgrid recipes in the two simulations, and may relate to early, efficient galaxy quenching in IllustrisTNG. This example again highlights the sensitivity (and constraining power) of SMG number counts and redshift distributions to the subgrid models employed in cosmological simulations.

The Feedback In Realistic Environments project (Hopkins et al. 2014, 2018b) provides an ideal set of high-resolution zoom-in simulations with which to derive new scaling relations. Crucially, these simulations resolve the formation of giant molecular clouds, which is currently not possible over cosmological volumes. The implementation of radiative transfer does not therefore require particle resampling, and the detailed geometry of stars and dust can be better resolved (assuming that the dust traces the gas with a fixed dust-to-metals mass ratio). Coupling with radiative transfer models has shown that these simulations produce galaxies with realistic sizes in the sub-millimetre (Cochrane et al. 2019). The focus of this paper is on deriving updated scaling relations to predict sub-millimetre flux densities using the FIRE-2 simulations.

The structure of this paper is as follows. In Section 2, we describe the FIRE simulations in detail and outline the radiative transfer methods used to make predictions for the rest-frame far-infrared (FIR) emission of each simulation snapshot. In Section 3, we show that the predicted scaling relations between dust mass, star formation rate, and observable sub-millimetre flux density are broadly consis-

Table 1. Properties of the eight simulated FIRE-2 haloes at $z = 3$. $M_{\rm halo}$ denotes the total mass of dark matter within the halo's virial radius, $R_{\rm vir}$. $M_\star$, $M_{\rm gas}$, $\rm SFR_{10}$, and S_{870} denote the stellar mass, gas mass, 10 Myr-averaged star formation rate, and observed-frame 870 μm flux density of the halo's central galaxy, all calculated within $0.1R_{\rm vir}$.

Name	$\log_{10} M_{\rm halo}$ ($\rm M_\odot$)	$\log_{10} M_\star$ ($\rm M_\odot$)	$\log_{10} M_{\rm gas}$ ($\rm M_\odot$)	$\log_{10} M_{\rm dust}$ ($\rm M_\odot$)	$\rm SFR_{10}$ ($\rm M_\odot yr^{-1}$)	S_{870} (mJy)
A1	12.17	10.98	10.11	8.04	133	0.65
A2	12.24	11.09	10.53	8.41	57	0.95
A4	11.91	10.29	10.22	7.70	61	0.23
A8	11.84	9.90	10.11	7.50	55	0.16
B1	11.71	10.64	10.19	7.78	46	0.32
B2	12.49	11.52	10.63	8.16	261	1.19
C1	12.77	11.66	10.62	7.76	382	0.80
C2	12.59	11.36	10.50	8.33	358	1.60

tent with a large, homogeneously selected observational sample of SMGs. We then use our simulations to derive a simple, analytical formula that enables us to make rapid predictions for sub-millimetre flux density from SFR and dust mass. We validate this new relation using the observational data. In Section 4, we extend this study to predict sub-millimetre flux densities at various wavelengths by also including stellar mass and redshift terms. We apply the model to galaxies in the EAGLE simulations in Section 5, discuss limitations in Section 6, and draw conclusions in Section 7.

2 HYDRODYNAMICAL SIMULATIONS AND RADIATIVE TRANSFER CALCULATIONS

2.1 Galaxies in the FIRE-2 simulations

The FIRE project (Hopkins et al. 2014, 2018b) is a suite of state-of-the-art hydrodynamical cosmological zoom-in simulations designed to explore the role of stellar feedback in galaxy formation and evolution. Without stellar feedback, the ISM would collapse on dynamical time-scales, leading to accelerated star formation. This is ruled out by the gas consumption time-scales of observed galaxies, as well as by galaxy stellar mass functions and the stellar mass–halo mass relation (see the overviews presented in Hopkins, Quataert & Murray 2011 and Somerville & Davé 2015). Galactic outflows are believed to regulate the mass of galaxies over time (Kereš et al. 2009; Faucher-Giguère et al. 2015; Anglés-Alcázar et al. 2017b) and to enrich the circumgalactic medium (see Hafen et al. 2019) and intergalactic medium (see the review by Rupke 2018). Numerous stellar feedback processes are believed to contribute, in a complex, non-linear manner. These include supernovae, protostellar jets, photoheating, stellar mass-loss from O- and AGB-stars and radiation pressure (see the review of Dale 2015). Cosmological zoom simulations have only recently achieved sufficient resolution to model these feedback processes directly.

Multichannel feedback is modelled by FIRE using two primary techniques. First, FIRE resolves the formation of giant molecular clouds (GMCs), with star formation taking place only in self-gravitating (according to the Hopkins, Narayanan & Murray 2013 criterion), self-shielding molecular gas (following Krumholz & Gnedin 2011) at high densities ($n_{\rm H} > 1000\,\rm cm^{-3}$ in the simulations we use here). Secondly, FIRE includes models for energy and momentum return from the main stellar feedback processes, with direct implementation of the predictions of stellar population synthesis models without parameter tuning. Once a star particle forms, the simulations explicitly follow several different stellar feedback mechanisms, as detailed in Hopkins et al. (2018a), including (1) local and long-range momentum flux from radiation pressure (in both the initial UV/optical single-scattering regime and re-radiated light in the IR); (2) energy, momentum, mass, and metal injection from SNe (Types Ia and II) and stellar mass-loss (both OB and AGB); and (3) photoionization and photoelectric heating. Every star particle is treated as a single stellar population with known mass, age, and metallicity. All feedback event rates, luminosities and energies, mass-loss rates, and all other quantities are tabulated directly from stellar evolution models (STARBURST99; Leitherer et al. 1999), assuming a Kroupa (2002) initial mass function. The FIRE prescription enables the self-consistent generation of galactic winds (Muratov et al. 2015; Anglés-Alcázar et al. 2017b; Pandya et al. 2021) and the reproduction of many observed galaxy properties, including stellar masses, star formation histories and the 'main sequence' of star-forming galaxies (see Hopkins et al. 2014; Sparre et al. 2017), metallicities and abundance ratios (van de Voort et al. 2015; Ma et al. 2016), as well as morphologies and kinematics of both thin and thick discs (Ma et al. 2018).

For this paper, we study the central galaxies of eight massive haloes originally selected and simulated by Feldmann et al. (2016, 2017) with the original FIRE model (Hopkins et al. 2014) as part of the MASSIVEFIRE suite. The first four of these are drawn from the 'A-series' of Feldmann et al. (2017) (A1, A2, A4, and A8). These haloes were selected to have dark matter halo masses of $M_{\rm halo} \sim 10^{12.5}\,\rm M_\odot$ at $z = 2$. The central galaxies of these haloes have stellar masses of 7×10^{10} to $3 \times 10^{11}\,\rm M_\odot$ at $z = 2$ (detailed in Table 1), with a variety of formation histories; see Feldmann et al. (2017) for details. The subset of four A-series haloes studied in this paper are drawn from Anglés-Alcázar et al. (2017c), who re-simulated them down to $z = 1$ with the upgraded FIRE-2 physics model (Hopkins et al. 2018b) and with a novel on-the-fly treatment for the seeding and growth of supermassive black holes (SMBHs; see Anglés-Alcázar et al. 2017a for details of the gravitational torque-driven model). Compared to FIRE-1, FIRE-2 simulations are run with a new, more accurate hydrodynamics solver (a mesh-free Godunov solver implemented in the GIZMO[1] code; Gaburov & Nitadori 2011; Hopkins 2015). They also feature improved treatments of cooling and recombination rates, gravitational softening and numerical feedback coupling, and they adopt a higher density threshold for star formation (Hopkins et al. 2018a). Note that these simulations do not include feedback from the accreting SMBHs.[2] A small number of snapshots from these haloes

[1] http://www.tapir.caltech.edu/~phopkins/Site/GIZMO.html

[2] Given that in extreme cases, AGN can be the dominant driver of cold dust emission (McKinney et al. 2021), it would be interesting to repeat our analyses with simulations including AGN feedback and emission in future work. However, we expect this effect to be unimportant for the bulk of the population.

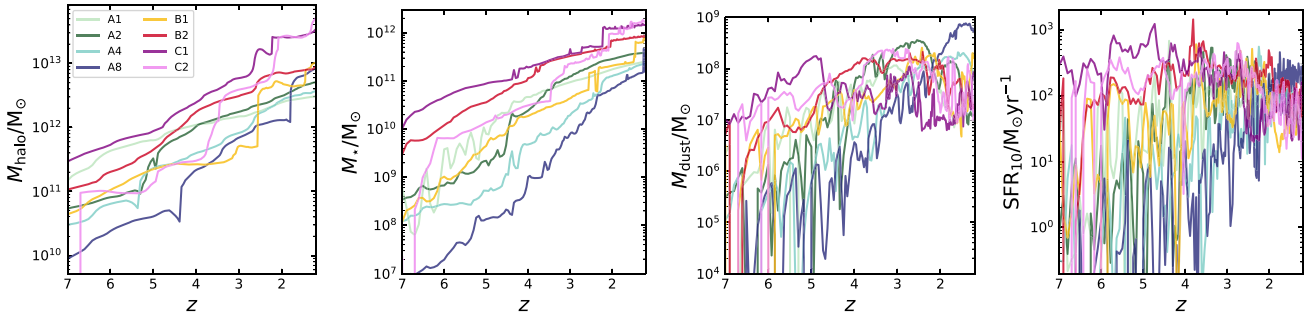

Figure 1. The evolution of physical quantities of the eight FIRE-2 haloes used in this paper. From left to right: evolution of halo mass; evolution of stellar mass within 0.1 R_{vir}; evolution of dust mass within 0.1 R_{vir} (note that this is calculated by weighting the mass of metals in the gas phase by a constant dust-to-metals mass ratio); and evolution of 10 Myr-averaged star formation rate. The haloes display a variety of dark matter and stellar mass growth histories. Haloes C1 and C2 are the most massive, reaching $M_{halo} > 10^{13}$ M$_\odot$ by $z = 2$.

were also studied in Cochrane et al. (2019) and Parsotan et al. (2021). For this study, we supplement the four 'A-series' haloes by re-running four more haloes from Feldmann et al. (2017), with the updated FIRE-2 physics. Two of the haloes are drawn from their 'B-series' (B1 and B2) and two from the 'C-series' (Cm1:0, hereafter C1, and C2:0, hereafter C2). The B and C series haloes were selected to have dark matter halo masses of $M_{halo} \sim 10^{13}$ M$_\odot$ and $M_{halo} \sim 10^{13.5}$ M$_\odot$ at $z = 2$, respectively. For these four haloes, we do not implement black hole seeding or growth. In Fig. 1, we show the evolution of the halo mass of each of the eight haloes, as well as the evolution of the stellar mass, dust mass, and star formation rate of their central galaxies.

The mass resolution of our A-series simulations is 3.3×10^4 M$_\odot$ for gas and star particles and 1.7×10^5 M$_\odot$ for dark matter particles (high resolution, hereafter HR). The mass resolution of our B-series simulations is 2.7×10^5 M$_\odot$ for gas and star particles and 1.4×10^6 M$_\odot$ for dark matter particles (standard resolution, hereafter SR). The mass resolution of our C-series simulations is 2.2×10^6 M$_\odot$ for gas and star particles and 1.1×10^7 M$_\odot$ for dark matter particles (low resolution, hereafter LR). We describe the resolution tests in Appendix A, and show that even the lowest resolution simulations are converged.

2.2 Performing radiative transfer to predict realistic galaxy fluxes

Modelling the multiwavelength emission from simulated galaxies can be challenging due to the need to account for the complex three-dimensional spatial distribution of radiation sources (stars and AGNs), and the dust particles that scatter, absorb, and re-emit light. Performing the detailed radiative transfer modelling necessary can be computationally expensive (see Steinacker, Baes & Gordon 2013, for a review).

In this work, we follow the methods described in Cochrane et al. (2019) to apply the Stellar Kinematics Including Radiative Transfer (SKIRT)[3] Monte Carlo radiative transfer code (Baes et al. 2011; Camps & Baes 2015) to FIRE-2 galaxies in post-processing. Monte Carlo radiative transfer codes like SKIRT treat the radiation field as a flow of photons through the dusty medium of a galaxy to compute the effects of dust absorption, scattering, and re-emission of the absorbed light, including dust self-absorption. While Cochrane et al. (2019) selected only the most sub-millimetre bright snapshots for their analysis, we have run SKIRT on all simulation snapshots for each of the eight haloes studied. We briefly summarize the method here.

Gas and star particles (along with their properties such as age and metallicity) are drawn from the FIRE-2 simulations at each snapshot. Prior to input to SKIRT, we rotate the particles to align the line of sight with the angular momentum vector of the gas particles within $0.1R_{vir}$, such that the galaxy is 'face on' (for disc galaxies) at a viewing angle of 0 degrees. Dust particles are assumed to follow the distribution of the metals, with a dust-to-metals mass ratio of 0.4 (Dwek 1998; James et al. 2002). We assume dust destruction at $> 10^6$ K (Draine & Salpeter 1979; Tielens et al. 1994). We model a mixture of graphite, silicate and PAH grains using the Weingartner & Draine (2001) Milky Way dust prescription. Star particles are assigned Bruzual & Charlot (2003) SEDs based on their ages and metallicities, assuming a Chabrier (2003) IMF. We use an octree dust grid, in which cell sizes are adjusted according to the dust density distribution, with the condition that no dust cell may contain more than 0.0001 per cent of the total dust mass of the galaxy. We use 10^6 photon packages, following tests that show convergence (see Appendix B).

The SKIRT output at a given modelled source orientation comprises spatially resolved images (on a grid with pixel side length 25 pc) at ∼100 discrete rest-frame wavelengths, spaced uniformly in log(wavelength) between rest-frame UV and FIR wavelengths. We also add the rest-frame wavelength corresponding to each ALMA band, for each snapshot (i.e. different rest-frame wavelengths that depend on the redshift of the snapshot). We model seven detectors at different orientations with respect to the disc plane of the galaxy. The field of view is set to 10 per cent of the virial radius for each galaxy snapshot studied. Tests confirm that this radius encloses all the sub-millimetre flux density from the simulated galaxy, even at the highest redshifts studied, where the virial radius is smallest.

Although SKIRT provides predictions for UV-FIR fluxes, in this paper, we focus on observed-frame sub-millimetre emission. The measured emission at these wavelengths is insensitive to orientation since we are usually in the optically thin regime (e.g. Cochrane et al. 2019), so we consider just the 'face-on' SKIRT-generated SED. In Fig. 2, we plot the evolution of the predicted (observed-frame) 870 μm flux density, S_{870}, SFR, and dust mass, for each of the eight simulated haloes. All physical quantities are calculated within a 3D aperture of radius 0.1 R_{vir}.

3 SCALING RELATIONS BETWEEN S_{870}, SFR, AND DUST MASS

In this section, we derive a simple power-law scaling relation between SFR, dust mass, and 870 μm flux density. First, we establish that the

[3] http://www.skirt.ugent.be

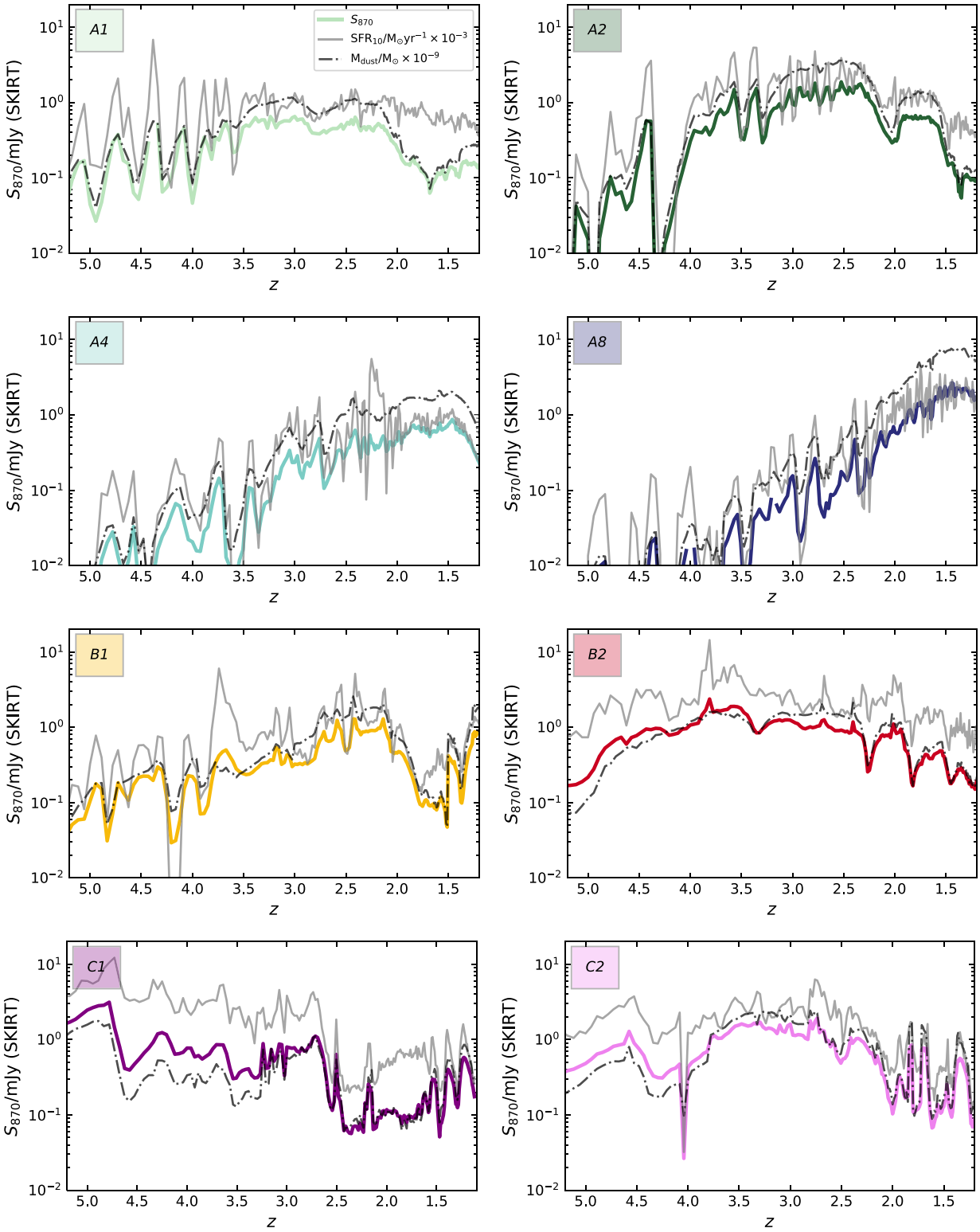

Figure 2. The redshift evolution of star formation rate (averaged over 10 Myr), dust mass, and SKIRT-predicted 870 μm flux density for the eight FIRE-2 central galaxies simulated, all calculated within 3D apertures of radius 0.1 R_{vir}. The galaxies display a range of star formation histories and 870 μm flux densities, with the most sub-millimetre bright snapshots reaching ∼3 mJy. At early times, feedback from bursty star formation expels gas; the derived dust mass hence varies on relatively short time-scales.

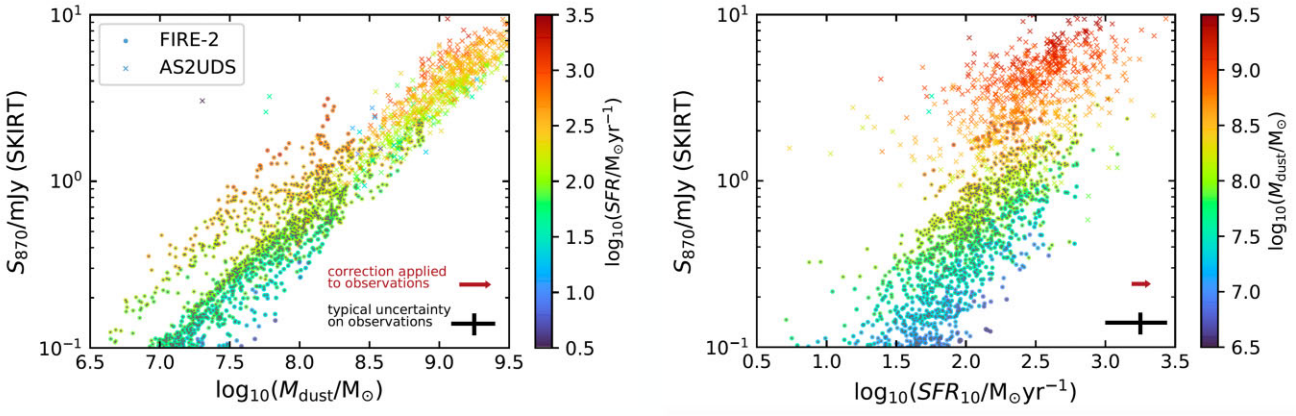

Figure 3. Left: SKIRT-predicted (observed-frame) 870 μm flux density versus dust mass, colour-coded by the 10 Myr-averaged star formation rate of the eight FIRE-2 haloes. Right: SKIRT-predicted (observed-frame) 870 μm flux density versus SFR, colour-coded by dust mass (we add small grey dots in the centre of each of these symbols, to aid visibility). We also show observational data from the AS2UDS sample (primarily comprising $S_{870} > 1$ mJy sources; Dudzeviciute et al. 2020), on the same colour-scale. Dust masses and SFRs are derived for the AS2UDS sources using the MAGPHYS SED fitting code, with small corrections applied to account for systematic bias. These are shown here with brown arrows: ∼0.2 dex for $M_{\rm dust}$ and ∼0.1 dex for SFR, as derived by Dudzeviciute et al. (2020). Typical uncertainties for the observationally derived parameters and flux densities are shown in black. The observational data are broadly consistent with the predictions based on applying SKIRT to our simulated galaxies. It is clear that S_{870} depends on both dust mass and star formation rate. At fixed dust mass, galaxies with higher star formation rates have higher S_{870}. At fixed star formation rate, galaxies with larger dust masses also have higher S_{870}.

FIRE-2 galaxies broadly follow the same trends in SFR–S_{870} and $M_{\rm dust}$–S_{870} as observed galaxies. In Fig. 3, we plot dust mass and SFR against SKIRT-predicted S_{870} for all snapshots studied for each of the eight haloes. We overplot observational data from the AS2UDS sample of ∼700 sub-millimetre sources (Dudzeviciute et al. 2020), homogeneously selected from the SCUBA-2 Cosmology Legacy Survey 850 μm map of the UKIDSS/UDS field (Stach et al. 2019). Dudzeviciute et al. (2020) use the MAGPHYS SED fitting code to infer dust mass and SFR from UV-radio photometry. Dudzeviciute et al. (2020) test the reliability of the MAGPHYS-derived quantities by fitting mock photometry of simulated EAGLE galaxies with known physical properties. They thereby infer correction factors ('true' dust mass is a factor of 1/0.65 higher than derived by MAGPHYS, while 'true' SFR is a factor of 1/0.8 higher). We apply these correction factors to their derived estimates. From these plots, it is clear that our predictions are in reasonable agreement with the observationally derived relations, though we do not reach the brightest sub-millimetre flux densities observed in AS2UDS, due to the limited parameter space probed by our small set of simulations (in particular, we do not reach extremely high values of SFR or $M_{\rm dust}$).

As seen from Fig. 3, it is clear from both observations and our simulations that both dust mass and SFR correlate with S_{870}. Neither dust mass nor SFR predicts S_{870} alone: at fixed dust mass, galaxies with higher star formation rates have higher S_{870}, and at fixed star formation rate, galaxies with larger dust masses also have higher S_{870}. In Section 3.1, we fit a power-law relation to relate the three quantities.

3.1 Predicting S_{870} from SFR and dust mass for FIRE galaxies

Following Hayward et al. (2011), we fit the following relation using the *emcee* package (Foreman-Mackey et al. 2013):

$$S_{870}/{\rm mJy} = \alpha \left(\frac{{\rm SFR}_{10}}{100\,{\rm M}_\odot{\rm yr}^{-1}} \right)^{\beta} \left(\frac{M_{\rm dust}}{10^8\,{\rm M}_\odot} \right)^{\gamma}. \quad (1)$$

Here, $\rm SFR_{10}$ corresponds to the star formation rate averaged over the 10 Myr before the snapshot; this approximately corresponds to the time-scales probed by observable SFR tracers (e.g. Flores Velázquez et al. 2021). $M_{\rm dust}$ is the total dust mass used by SKIRT in the radiative transfer. We were motivated to adopt this functional form due to its success in fitting radiative transfer-predicted flux densities previously (Hayward et al. 2011, 2013b) and its simplicity.

We present our results in Fig. 4. The derived parameters are $\alpha = 0.55 \pm 0.04$, $\beta = 0.50 \pm 0.09$, and $\gamma = 0.51 \pm 0.06$. Hayward et al. (2011) derived $\alpha = 0.65$, $\beta = 0.42$, and $\gamma = 0.58$. We overplot their results in blue. Lovell et al. (2021) perform a similar fit to galaxies in SIMBA, and obtain $\alpha = 0.58$, $\beta = 0.51$, and $\gamma = 0.49$. We overplot their results in green. No uncertainties are provided by either of these works. While the estimates of Lovell et al. (2021) are within $1\,\sigma$ of ours, those of Hayward et al. (2011) deviate more. The correlations between the fitted parameters shown in Fig. 4 help explain some discrepancies. While their estimate of β is $\sim 1\,\sigma$ lower than ours, their estimate of γ is $\sim 1\,\sigma$ greater. This makes sense given the negative correlations between the two parameters shown in 4. Their value of α deviates from ours by over $2\,\sigma$. Despite these differences, it is encouraging that the derived relations agree to the degree that they do; Hayward et al. (2011), for example, used highly idealized simulations with less sophisticated models for star formation, the ISM and stellar feedback.

In Fig. 5, we compare the sub-millimetre flux densities predicted by our formula to the flux densities derived using the radiative transfer, for the FIRE galaxy snapshots used in deriving the scaling relation. This shows how well the combination of $\rm SFR_{10}$ and dust mass can predict sub-millimetre flux density. For galaxies with $S_{870} > 0.1$ mJy, the mean $S_{870,\rm SKIRT}/S_{870,\rm formula}$ is 1.017. The standard deviation is 0.21. This indicates that S_{870} can typically be predicted to within 0.09 dex from the star formation rate and dust mass of a simulated galaxy alone. The tightness of this relation is encouraging. We explore the validity of application to other simulations in our application of FIRE-derived scaling relations to EAGLE galaxies in Section 5.

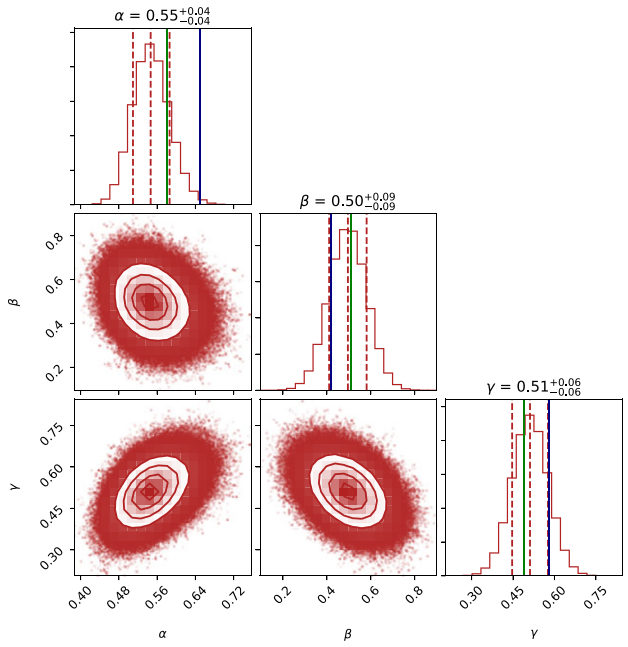

Figure 4. The posterior distribution of the parameters α, β, and γ, as described in equation (1), fitted to the FIRE-2 snapshots (using a *corner* plot; Foreman-Mackey 2016). Parameter estimates from Hayward et al. (2011) and Lovell et al. (2021) are overplotted in blue and green, respectively. Our fits show clear degeneracies between the fitted parameters, which may help understand discrepancies among previous fits.

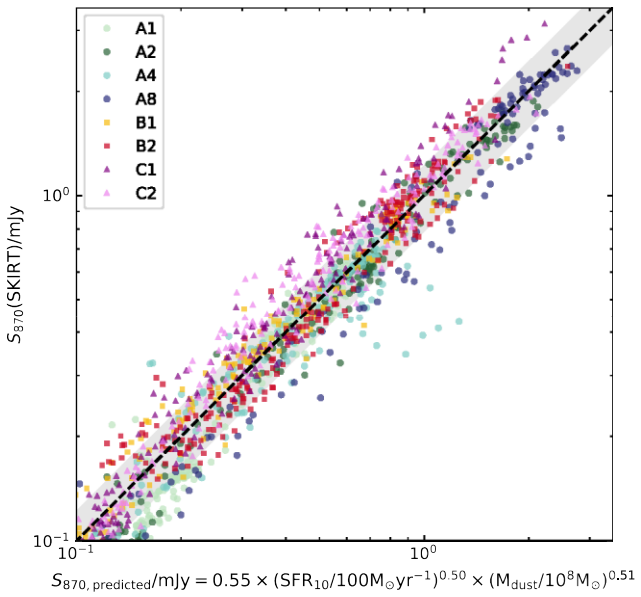

Figure 5. The SKIRT-predicted 870 μm flux density versus the value predicted by SFR_{10} and dust mass using our fitted formula, for all snapshots with $S_{870} > 0.1$ mJy, colour-coded by halo. For snapshots where $S_{870} > 0.1$ mJy, the mean $S_{870,\mathrm{SKIRT}}/S_{870,\mathrm{formula}}$ is 1.017. The standard deviation in $S_{870,\mathrm{SKIRT}}/S_{870,\mathrm{formula}}$ (plotted as the grey shaded region) is 0.21. This indicates that $S_{870\,\mu\mathrm{m}}$ can typically be predicted to within 0.09 dex from the star formation rate and dust mass of a simulated galaxy alone.

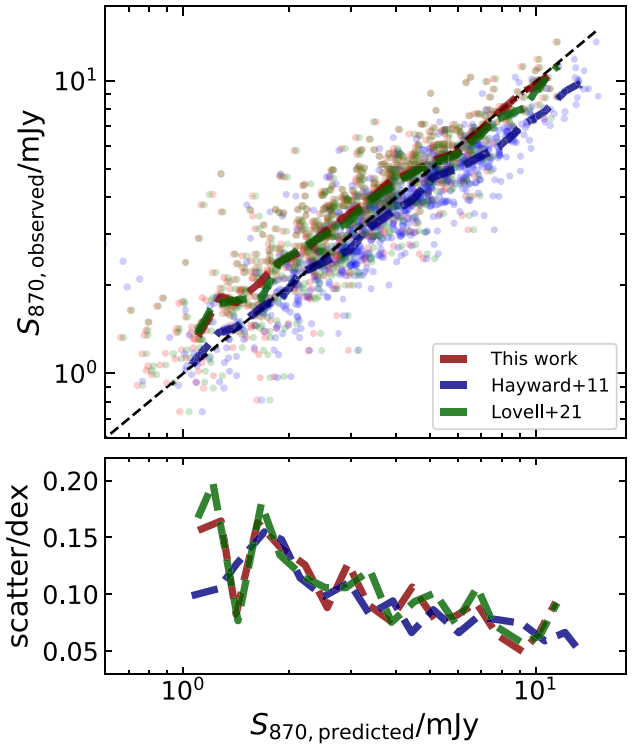

Figure 6. Upper panel: 870 μm flux density observed by ALMA against that predicted using dust mass and SFR (MAGPHYS estimates) for the AS2UDS galaxies. The flux densities predicted from the MAGPHYS-derived dust mass and SFR using our FIRE-derived scaling relation are in good agreement with those observed by ALMA, with median $S_{870,\mathrm{observed}}/S_{870,\mathrm{formula}} = 1.22$. Lower panel: the standard deviation in observed-to-predicted flux densities. The dashed lines on both panels show running medians (using 20 bins, log-spaced between 0 and 15 mJy), highlighting both the low scatter and the lack of strong trends with flux density.

3.2 Comparison with observational data

To validate our power law relation, we apply it to the (systematic bias-corrected) dust mass and SFR values predicted by MAGPHYS for the AS2UDS galaxies. In Fig. 6 (upper panel), we show observed versus predicted flux densities. The median value of $S_{870,\mathrm{observed}}/S_{870,\mathrm{formula}}$ is 1.22 (see middle panel). The standard deviation in $S_{870,\mathrm{observed}}/S_{870,\mathrm{formula}}$ is shown in the lower panel and is fairly constant with observed flux density, remaining at $\sim$0.1 dex. This adds confidence that our simulation-derived relations are consistent with those of real observed galaxies. Note that without the correction for bias in the MAGPHYS-inferred physical properties, the $S_{870,\mathrm{observed}}$ is systematically higher than predicted by the relation by $\sim$0.2 dex.

4 EXTENSION TO OTHER FIR/SUB-MILLIMETRE FLUX DENSITIES

Following the success of our simple power-law scaling between star formation rate, dust mass, and 870 μm flux density, presented in Section 3, we attempt to predict the FIR SED at more wavelengths via a similar parametrization. We develop a model that may be applied to the global properties of simulated galaxies to make rapid predictions for galaxy number counts at various sub-millimetre wavelengths. These simulated galaxies could include large box simulations, for which running radiative transfer would be computationally infeasi-

Table 2. Parameters in equation (2) fitted using FIRE-2 snapshots at $1 < z < 4$. The estimate for each parameter is the median of its posterior distribution, with $1\,\sigma$ uncertainties calculated using the 16th and 84th percentiles.

λ (μm)	$\log_{10}\alpha$	β	δ	γ	η
345	0.86 ± 0.02	0.49 ± 0.01	0.46 ± 0.02	0.19 ± 0.01	-0.86 ± 0.03
462	0.31 ± 0.03	$0.43^{+0.01}_{-0.02}$	0.53 ± 0.02	0.18 ± 0.01	-0.18 ± 0.05
652	$-0.29^{+0.09}_{-0.08}$	0.36 ± 0.04	$0.60^{+0.03}_{-0.04}$	0.15 ± 0.03	0.36 ± 0.11
870	-0.77 ± 0.2	0.32 ± 0.08	0.65 ± 0.07	0.13 ± 0.07	0.65 ± 0.25

ble; simulations with lower resolution (and more poorly resolved ISM) for which the output of radiative transfer may be unreliable; and SAMs, where detailed spatial distributions of stars and dust do not exist.

We fit the following relation to SKIRT-predicted observed-frame flux densities at 345, 462, 652, and 870 μm (corresponding to ALMA Bands 10, 9, 8, and 7, respectively), for snapshots in the redshift range $1 < z < 4$:

$$S_\nu/\mathrm{mJy} = \alpha \left(\frac{\mathrm{SFR}_{10}}{100\,\mathrm{M_\odot yr^{-1}}}\right)^{\beta} \left(\frac{M_\star}{10^{10}\,\mathrm{M_\odot}}\right)^{\gamma} \left(\frac{M_\mathrm{dust}}{10^{8}\,\mathrm{M_\odot}}\right)^{\delta} (1+z)^{\eta}. \quad (2)$$

Redshift is an important added parameter in this extension to other wavelengths, since we are fitting various observed-frame wavelengths and hence cannot rely on the negative *K*-correction for redshift-independence. As in Section 3.1, we use the SFR averaged over the 10 Myr prior to each snapshot. We again use the *emcee* package. Our best-fitting parameters are presented in Table 2 and plotted as a function of wavelength in Fig. 7. We note the following trends in fitted parameters with wavelength. The normalization factor, α, decreases with increasing wavelength, in line with the expected decrease in flux density with wavelength. β decreases with increasing wavelength, reflecting the increased role of SFR in determining sub-millimetre flux density around the peak of the dust SED. δ increases with wavelength, reflecting the increasing dominance of dust mass in driving sub-millimetre flux density as one approaches the Rayleigh–Jeans tail (see also Cochrane et al. 2022). γ is low ($\sim$0.1–0.2 dex) at all wavelengths, showing the weak dependence of sub-millimetre flux density on stellar mass. η increases with wavelength, in line with expectations from the negative *K*-correction.

Our derived scaling relations recover the SKIRT-derived flux densities accurately at all four wavelengths. Median values of offsets and scatter are $[-0.008, 0.11]$, $[-0.012, 0.087]$, $[-0.009, 0.071]$, and $[0.0011, 0.061]$ dex, for 345, 462, 652, and 870 μm, respectively. Using our scaling relations, the majority of the flux densities are predicted to within 0.1 dex, with no strong trends with flux density (see Fig. 8). In Section 5, we apply the derived relations to simulated galaxies from EAGLE.

5 APPLICATION OF THE FIRE-TRAINED RELATIONS TO THE EAGLE SIMULATION

5.1 The EAGLE simulation

The Virgo Consortium's Evolution and Assembly of GaLaxies and their Environments project (EAGLE[4]; Crain et al. 2015; Schaye et al. 2015) comprises a suite of Lambda cold dark matter simulations based on a modified version of the GADGET 3 SPH code (Springel et al. 2005). The simulations use subgrid models for radiative cooling, star formation, stellar mass-loss and metal enrichment, gas accretion onto black holes, black hole mergers, and energy feedback from both massive stars and AGNs. Feedback models are calibrated to the observationally inferred $z = 0.1$ galaxy stellar mass function, the galaxy stellar mass–size relation, and the galaxy–black hole mass relation (Crain et al. 2015). EAGLE reproduces a number of other observed galaxy relations (among them, distributions of specific star formation rate, passive fractions, the evolution of the stellar mass function, galaxy rotation curves, and the Tully–Fisher relation), despite not being explicitly calibrated to match them (Schaller et al. 2015; Schaye et al. 2015; Trayford et al. 2015; Furlong 2017).

The various simulations within the EAGLE suite are presented in McAlpine et al. (2016). We draw our galaxy samples from the largest box (version Ref-L100N1504; comoving side length 100 Mpc, 7 billion particles) to give the best number statistics. We select galaxies within the redshift range $1.5 < z < 4$. For the version of the EAGLE simulation we use, the particle mass resolution for gas is $1.81 \times 10^6\,\mathrm{M_\odot}$, and the particle mass resolution for dark matter is $9.71 \times 10^6\,\mathrm{M_\odot}$. The resolution was chosen to marginally resolve the Jeans mass of the gas at the star formation threshold. The comoving (Plummer equivalent) gravitational softening length is 2.66 kpc. Since EAGLE is a large box cosmological simulation, its resolution is low compared to the HR and SR FIRE zoom-ins.

5.2 Modelled sub-millimetre flux densities for EAGLE galaxies

We draw synthetic fluxes for the EAGLE galaxies from the 'DustyFluxes' table, which is part of the public data base. These observed-frame fluxes were generated following the methods described in Camps et al. (2018), which we summarize here. For each galaxy, gas and star particles were extracted within 30 proper kpc of the centre of mass of the star particles. Although the EAGLE project also uses the SKIRT radiative transfer code to generate galaxy SEDs, their methods of generating the intrinsic stellar emission differ from ours (primarily due to the lower particle mass resolution of EAGLE). Star particles with ages < 100 Myr and gas particles with non-zero SFRs were re-sampled into a number of sub-particles. These sub-particles have lower masses, drawn randomly from a mass distribution function chosen based on observations of molecular clouds in the Milky Way. Each sub-particle has a random formation time, assuming constant SFR over the previous 100 Myr. Of the generated set of sub-particles, those with assigned ages < 10 Myr define a set of 'star-forming' particles input separately to the radiative transfer. Older sub-particles were added to the set of star particles with ages > 100 Myr. Gas sub-particles that have not yet formed stars were added to the set of gas particles with zero SFR. There were then three inputs to the SKIRT radiative transfer: stars with ages > 90 Myr, stars with ages < 10 Myr, and gas.

[4] http://icc.dur.ac.uk/Eagle/

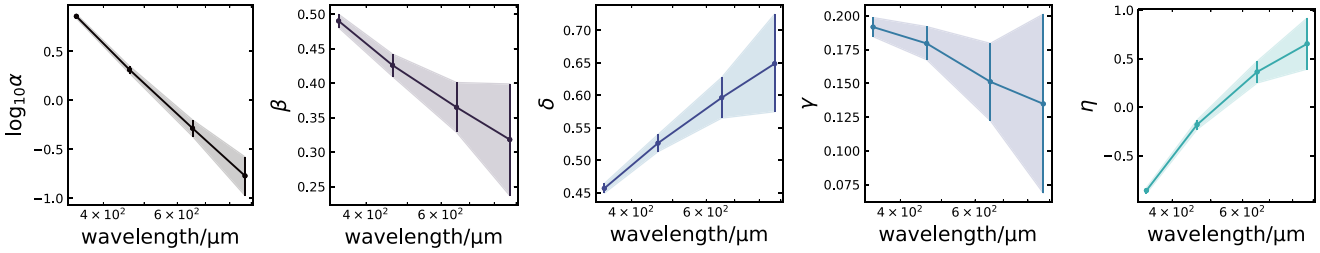

Figure 7. Parameters of $S_\nu/\mathrm{mJy} = \alpha \left(\frac{\mathrm{SFR}_{10}}{100\,\mathrm{M_\odot yr^{-1}}}\right)^{\beta} \left(\frac{M_{\mathrm{dust}}}{10^8\,\mathrm{M_\odot}}\right)^{\delta} \left(\frac{M_\star}{10^{10}\,\mathrm{M_\odot}}\right)^{\gamma} (1+z)^{\eta}$ fitted using FIRE-2 snapshots at $1 < z < 4$. The estimate for each parameter is the median of its posterior distribution, with $1\,\sigma$ uncertainties calculated using the 16th and 84th percentiles. We use the 10 Myr-averaged SFR. Notably, β decreases with increasing wavelength, reflecting the increasing importance of SFR in determining sub-millimetre flux density closer to the peak of the dust SED. δ displays the opposite trend, reflecting the increasing dominance of dust mass in driving sub-millimetre flux density at longer wavelengths.

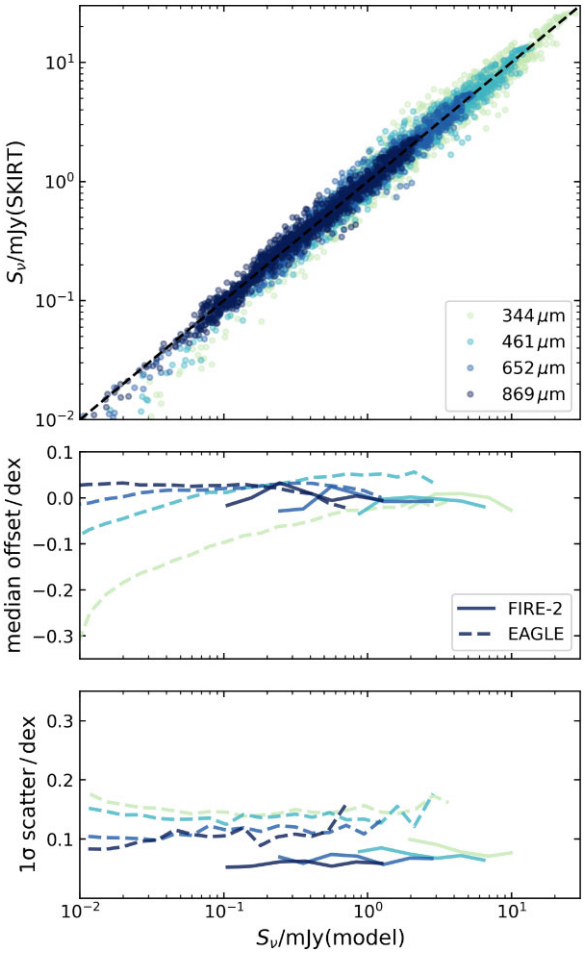

Figure 8. Top panel: SKIRT-predicted versus model-predicted flux density for ALMA Bands 7, 8, 9, and 10, for the FIRE-2 snapshots. Middle panel: running median offset from the model-predicted flux density for the FIRE-2 galaxies (solid lines) and EAGLE galaxies (dashed lines). Bottom panel: running scatter in the relation shown in the upper panel. The flux densities predicted for EAGLE galaxies using our scaling relations are typically within 0.2 dex of the SKIRT-predicted values.

Within SKIRT, dust was modelled based on the 'cold' gas particles (those with a non-zero SFR or temperature $T < 8000$ K), assuming a dust-to-metals mass fraction of 0.3 and a Zubko, Dwek & Arendt (2004) dust model. SEDs were assigned to stellar particles with ages > 90 Myr using Bruzual & Charlot (2003) models, taking into account mass, metallicity, and age. Younger star particles were assigned starburst SEDs from the MAPPINGS III family (Groves et al. 2008; Jonsson et al. 2010), which aims to model the H II regions as well as the photodissociation regions (PDRs). Each young particle was also assigned a position based on the position and smoothing length of its parent particle. Since dust is partially modelled by the MAPPINGS implementation of the PDR, the implicit PDR dust masses were subtracted from the diffuse dust distribution surrounding the star-forming region (otherwise this dust would be 'double counted'). The radiative transfer was then performed on an octree grid.

5.3 Rapid predictions of number counts using the trained scaling relations

In this section, we apply the scaling relations derived using FIRE galaxies (as described in Section 4) to EAGLE galaxies, generating predicted flux densities in four ALMA bands for each EAGLE galaxy. We generate number counts using these predicted flux densities, as well as using the flux densities derived directly from the application of SKIRT to EAGLE described in Section 5.2, and compare the resulting number counts.

We first select EAGLE galaxies in the redshift range $1.5 < z < 4$. We input the relevant features for each of the ∼80 000 EAGLE snapshots in the sample to the scaling relations derived in Section 4. Note that although EAGLE have used a different dust-to-metals mass ratio in their calculation of dust mass (0.3, compared to our 0.4), this does not affect the robustness of our flux density estimates because the dust mass rather than the gas mass is used in our scaling relation. The process of predicting the flux densities that would be observed at the wavelengths of the various ALMA bands, for all EAGLE snapshots, from the dust mass, star formation rate, stellar mass and redshift takes just a few minutes on a laptop.

We compare the flux densities predicted using our scaling relations to those predicted using SKIRT. We show the median difference between model and SKIRT-predicted flux density values, as a function of model-predicted flux density, in the middle panel of Fig. 8. Encouragingly, there is no significant bias (i.e. the median offset is ∼0), except at the shortest wavelength studied, where SKIRT predicts lower flux densities than our relations for the faintest sources. The scatter in this relation is shown in the lower panel of Fig. 8. The scatter for EAGLE galaxies is low, within 0.2 dex across over two orders of magnitude of flux density, for all wavelengths studied. The success of our FIRE-derived scaling relations in predicting the flux densities for

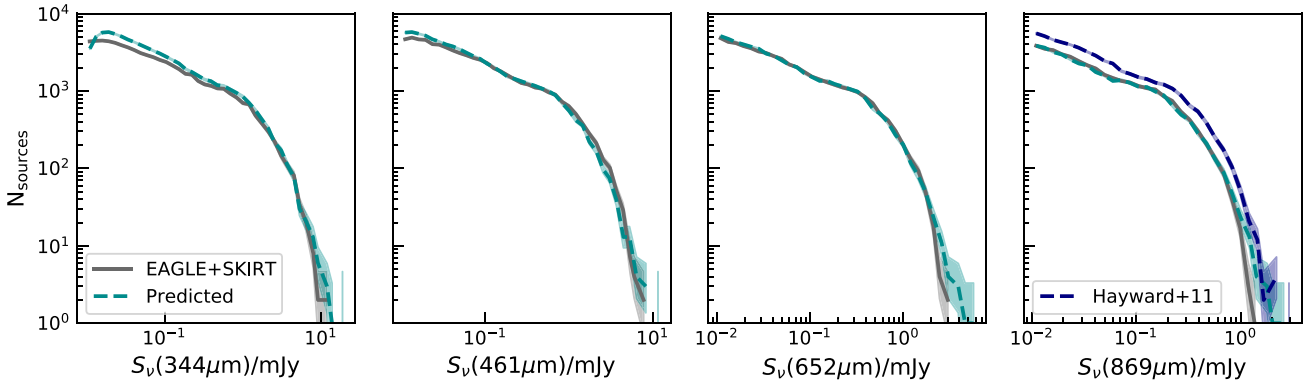

Figure 9. Number counts at $1.5 < z < 4$ for four sub-millimetre wavelengths, as predicted by the scaling relations from the following properties of the EAGLE galaxies: dust mass, stellar mass, SFR, and redshift (dark cyan). In light cyan, we show Poisson uncertainties [calculated using single-sided errors drawn from Gehrels (1986) for cases where $N < 100$]. In dark grey, we show the number counts predicted by running the SKIRT radiative transfer code on the EAGLE galaxies. The grey shaded region shows Poisson uncertainties. The number counts generated using our scaling relations are generally very similar to those yielded by performing radiative transfer on the EAGLE galaxies. This shows that our scaling relations can be applied to other simulations and semi-analytical or semi-empirical models and quickly generate robust predictions for number counts, even when these other simulations have different input physics and particle resolutions. We overlay the 870 μm number counts predicted using the scaling relation derived by Hayward et al. (2011) in blue. These overpredict the EAGLE + SKIRT-derived counts by ∼20 per cent.

EAGLE galaxies is notable. It means that, for galaxies drawn from EAGLE and FIRE with a given set of physical parameters (dust mass, stellar mass, star formation rate, and redshift), SKIRT predicts very similar sub-millimetre flux density values, despite the different input physics, subgrid models, and resolutions of the two simulations. This is encouraging for the broader application of the scaling relations.

We display the number counts predicted by the scaling relations and those derived directly from EAGLE + SKIRT in Fig. 9. These show excellent agreement, in general to within Poisson uncertainties (unlike those derived using the scaling relation derived by Hayward et al. 2011, which overpredict counts by ∼20 per cent at all flux densities). We marginally overpredict bright sources, possibly due to Eddington (1913) bias. The overall success of our scaling relations is particularly encouraging given that they were trained on simulations with different input physics and resolutions, and with slightly different radiative transfer set-up. This shows that our scaling relations can be applied to other simulations and semi-analytical or semi-empirical models to generate robust and fast predictions for number counts.

6 DISCUSSION

Our FIRE-trained scaling relations are remarkably accurate in predicting sub-millimetre flux densities of EAGLE galaxies from global galaxy properties alone. They provide a promising path for rapid generation of sub-millimetre number counts where radiative transfer is infeasible. Here, we will discuss some limitations of our method and avenues for future work.

Although the FIRE-2 simulations used here succeed in reproducing many observed galaxy properties, including the compact sizes of massive SMGs (Cochrane et al. 2019), there remain some limitations to the model. First, as shown in Parsotan et al. (2021), the optical sizes of massive FIRE-2 galaxies are overcompact compared to the observationally derived size–stellar mass relation, particularly at $z < 2$. Less massive FIRE-2 galaxies do not display this issue (El-Badry et al. 2016). This is at least partially attributable to the lack of AGN feedback in the models; numerous works have shown that AGN-driven winds leave an impact on galaxy stellar sizes and densities (e.g. Choi et al. 2018; Zoldan et al. 2019; Van der Vlugt et al. 2021). Efforts to implement AGN feedback into the simulations have already begun (Wellons et al. 2022; Anglés-Alcázar et al., in preparation), and future work will explore the impact of AGN-driven winds on physical and observable galaxy sizes (Cochrane & Anglés-Alcázar, in preparation). An AGN feedback implementation would impact the evolution of stellar mass and star formation rate in a simulated massive galaxy. However, in this work we derive scaling relations to predict sub-millimetre flux density given some input physical quantities, so this work should be robust to changes in the details of the feedback models. The success of our model in predicting sub-millimetre number counts of galaxies drawn from the EAGLE simulations, which do include thermal AGN feedback (Schaye et al. 2015), supports this.

Secondly, although our radiative transfer method is well established and sophisticated compared to simple dust screen models, we do not model dust production, growth, or destruction in a self-consistent manner. In this paper, we use a fixed dust-to-metals ratio of 0.4; this assumption and slight variations in it are common in the post-processing of zoom and cosmological scale simulations (e.g. Camps et al. 2016; Liang et al. 2018, 2019; Cochrane et al. 2019; Trayford & Schaye 2019; Parsotan et al. 2021; Popping et al. 2022), though note that efforts to implement dust evolution in FIRE are ongoing (Choban et al. 2022). In SIMBA, which does include a model for on-the-fly dust production and destruction (following McKinnon et al. 2017), average dust masses are a factor of ∼2.5 higher than if this fixed dust-to-metals ratio had been applied (Lovell et al. 2021). These lead to more bright SMGs in SIMBA. Nevertheless, since dust mass is an input parameter to our scaling relations, the derived relations should not be highly sensitive to the exact values. Of more concern is the spatially invariant dust-to-metals ratio; observational results disagree about the validity of this assumption (see Chiang et al. 2018 and references therein). If the geometry of the dust is important for the flux densities and unrealistic, our scaling relations could be biased. However, the success of our model in bypassing radiative transfer for EAGLE galaxies, which are simulated at lower spatial resolution, points towards this being of negligible importance at the wavelengths studied.

We have limited the scope of this work to a small set of observed-frame sub-millimetre flux densities. As argued, sub-millimetre number counts and redshift distributions can provide an important

constraint to galaxy formation models. Ideally, though, our model would be generalizable to shorter wavelengths and able to make fast predictions for full galaxy SEDs. In future work, we will explore machine learning-based approaches to this problem.

7 CONCLUSIONS

In this paper, we have trained simple scaling relations between observable sub-millimetre flux densities of simulated high-redshift galaxies and combinations of their key intrinsic physical properties, including star formation rate, dust mass, stellar mass, and redshift. We use a set of high-resolution cosmological zoom-in simulations of massive, star-forming galaxies from the FIRE suite. We use SKIRT to perform radiative transfer on the simulated galaxies, thereby incorporating a realistic star–dust geometry (assuming that the dust-to-metals mass ratio is constant and does not vary spatially). We generate observed-frame galaxy SEDs, from which we extract predictions for the emission that would be measured by ALMA bands 10, 9, 8, and 7 (352–870 μm).

The primary aim of this project is to make use of our very high resolution and computationally expensive simulations to derive relations that can be applied to other models. Applications include large box simulations, for which running radiative transfer can be infeasible; lower-resolution (LR) simulations for which the star–dust geometry is inadequately resolved for robust SED prediction; and semi-analytical and semi-empirical models for which detailed spatial distributions of stars and dust do not exist. The relations we derive between physical properties (dust mass, stellar mass, SFR_{10}, and redshift) and 352–870 μm flux density have strong physical bases. At longer wavelengths, the dependence of flux density on dust mass increases, as would be expected as we move closer to the Rayleigh–Jeans regime. Star formation rate plays an increased role at shorter wavelengths, further from the Rayleigh–Jeans regime, where flux density is expected to depend superlinearly on dust temperature. At all wavelengths studied, flux density is only weakly dependent on stellar mass. The relations we derive are broadly consistent with previous work using both single halo idealized zooms and cosmological scale simulations; this indicates that global galaxy properties determine most of the variation in the sub-millimetre flux densities of galaxies.

We apply our derived scaling relations to galaxies from EAGLE, a large box cosmological hydrodynamical simulation. Importantly, radiative transfer has already been performed on these EAGLE galaxies, with SKIRT outputs provided as part of the publicly available online data base. We find that EAGLE sub-millimetre number counts derived using our simple scaling relations agree remarkably well with those constructed using the radiative transfer-derived flux densities. This provides confidence in the validity of the application of the scaling relations to simulations with very different resolutions and physics to FIRE-2. As highlighted by Cochrane et al. (2019), UV–optical emission is expected to be more strongly dependent on the resolved ISM geometry and viewing angle; predictions for emission at these shorter wavelengths thus strongly motivate detailed radiative transfer. In future work, we will explore methods to predict the entire UV–FIR galaxy SED from intrinsic galaxy properties.

ACKNOWLEDGEMENTS

We thank the anonymous reviewer, Caleb Choban, and Desika Narayanan for helpful comments on earlier versions of this paper. The Flatiron Institute is supported by the Simons Foundation. RKC is grateful for the support of the John Harvard Distinguished Science Fellowship. DAA was supported in part by NSF grants AST-2009687 and AST-2108944, and CXO grant TM2-23006X. The FIRE project is supported by the NSF and TACC, by grants AST21010 and AST20016.

DATA AVAILABILITY

The data underlying this article will be shared on reasonable request to the corresponding author.

REFERENCES

Anglés-Alcázar D., Davé R., Faucher-Giguère C.-A., Özel F., Hopkins P. F., 2017a, MNRAS, 464, 2840
Anglés-Alcázar D., Faucher-Giguère C.-A., Kereš D., Hopkins P. F., Quataert E., Murray N., 2017b, MNRAS, 470, 4698
Anglés-Alcázar D., Faucher-Giguère C. A., Quataert E., Hopkins P. F., Feldmann R., Torrey P., Wetzel A., Kereš D., 2017c, MNRAS, 472, L109
Baes M., Verstappen J., De Looze I., Fritz J., Saftly W., Vidal Pérez E., Stalevski M., Valcke S., 2011, ApJS, 196, 22
Barger A. J., Cowie L., Sanders D. B., Fulton E., Taniguchi Y., Sato Y., Kawara K., Okuda H., 1998, Nature, 394, 248
Baugh C. M., Lacey C. G., Frenk C. S., Granato G. L., Silva L., Bressan A., Benson A. J., Cole S., 2005, MNRAS, 356, 1191
Blain A. W., Smail I., Ivison R. J., Kneib J. P., Frayer D. T., 2002, Phys. Rep., 369, 111
Bouwens R. J., Stefanon M., Oesch P. A., Illingworth G. D., Nanayakkara T., Roberts-Borsani G., Labbé I., Smit R., 2019, ApJ, 880, 25
Bouwens R. et al., 2020, ApJ, 902, 112
Bouwens R. J. et al., 2021, ApJ, 162, 47
Bouwens R. J., Illingworth G., Ellis R. S., Oesch P., Paulino-Afonso A., Ribeiro B., Stefanon M., 2022, ApJ, 931, 81
Bruzual G., Charlot S., 2003, MNRAS, 344, 1000
Calistro Rivera G. et al., 2018, ApJ, 863, 56
Camps P., Baes M., 2015, Astron. Comput., 9, 20
Camps P., Trayford J. W., Baes M., Theuns T., Schaller M., Schaye J., 2016, MNRAS, 462, 1057
Camps P. et al., 2018, ApJ, 234, 20
Casey C. M. et al., 2018, ApJ, 862, 77
Chabrier G., 2003, PASP, 115, 763
Chen C.-C. et al., 2017, ApJ, 846, 108
Chen C.-C. et al., 2020, A&A, 635, A119
Chiang I.-D., Sandstrom K. M., Chastenet J., Johnson L. C., Leroy A. K., Utomo D., 2018, ApJ, 865, 117
Choban C. R., Hopkins D. K. P. F., Sandstrom K. M., Hayward C. C., Faucher-Giguère C.-A., 2022, MNRAS, 22, 1
Choi E., Somerville R. S., Ostriker J. P., Naab T., Hirschmann M., 2018, ApJ, 866, 91
Cochrane R. K. et al., 2019, MNRAS, 488, 1779
Cochrane R. K., Best P. N., Smail I., Ibar E., Cheng C., Swinbank A. M., Molina J., Sobral D., 2021, MNRAS, 503, 2622
Cochrane R. K., Hayward C. C., Anglés-Alcázar D., 2022, ApJ, 939, L27
Cole S. et al., 2000, MNRAS, 326, 255
Cowley W. I., Lacey C. G., Baugh C. M., Cole S., Frenk C. S., Lagos C. d. P., 2019, MNRAS, 487, 3082
Crain R. A. et al., 2015, MNRAS, 450, 1937
Da Cunha E. et al., 2015, ApJ, 806, 110
Dale J. E., 2015, New Astron. Rev., 68, 1
Davé R., Anglés-Alcázar D., Narayanan D., Li Q., Rafieferantsoa M. H., Appleby S., 2019, MNRAS, 486, 2827
Draine B. T., Salpeter E. E., 1979, ApJ, 231, 77
Dudzeviciute U. et al., 2020, MNRAS, 494, 3828
Dunlop J. S. et al., 2017, MNRAS, 466, 861
Dwek E., 1998, ApJ, 1, 643
Eddington A. S., 1913, MNRAS, 73, 359
El-Badry K., Wetzel A., Geha M., Hopkins P. F., Kereš D., Chan T. K., Faucher-Giguère C.-A., 2016, ApJ, 820, 131

Faucher-Giguère C. A., Hopkins P. F., Kereš D., Muratov A. L., Quataert E., Murray N., 2015, MNRAS, 449, 987
Feldmann R., Hopkins P. F., Quataert E., Faucher-Giguère C. A., Kereš D., 2016, MNRAS, 458, L14
Feldmann R., Quataert E., Hopkins P. F., Faucher-Giguére C. A., Kereš D., 2017, MNRAS, 470, 1050
Finkelstein S. L. et al., 2022, ApJ, 928, 52
Flores Velázquez J. A. et al., 2021, MNRAS, 501, 4812
Foreman-Mackey D., 2016, J. Open Source Softw., 1, 24
Foreman-Mackey D., Hogg D. W., Lang D., Goodman J., 2013, PASP, 125, 306
Fujimoto S. et al., 2021, ApJ, 911, 99
Furlong M., 2017, MNRAS, 465, 722
Gaburov E., Nitadori K., 2011, MNRAS, 414, 129
Garcia-Vergara C., Hodge J., Hennawi J. F., Weiss A., Wardlow J., Myers A. D., Hickox R., 2020, ApJ, 904, 2
Gehrels N., 1986, ApJ, 303, 336
Genel S. et al., 2014, MNRAS, 445, 175
Granato G. L., Lacey C. G., Silva L., Bressan A., Baugh C. M., Cole S., Frenk C. S., 2000, ApJ, 542, 710
Groves B., Dopita M. A., Sutherland R. S., Kewley L. J., Fischera J., Leitherer C., Brandl B., van Breugel W., 2008, ApJS, 176, 438
Hafen Z. et al., 2019, MNRAS, 488, 1248
Hayward C. C., Kereš D., Jonsson P., Narayanan D., Cox T. J., Hernquist L., 2011, ApJ, 743, 159
Hayward C. C., Jonsson P., Kereš D., Magnelli B., Hernquist L., Cox T. J., 2012, MNRAS, 424, 951
Hayward C. C., Narayanan D., Kereš D., Jonsson P., Hopkins P. F., Cox T. J., Hernquist L., 2013a, MNRAS, 428, 2529
Hayward C. C., Behroozi P. S., Somerville R. S., Primack J. R., Moreno J., Wechsler R. H., 2013b, MNRAS, 434, 2572
Hayward C. C. et al., 2018, MNRAS, 476, 2278
Hayward C. C. et al., 2021, MNRAS, 502, 2922
Hickox R. C. et al., 2012, MNRAS, 421, 284
Hodge J. A., da Cunha E., 2020, R. Soc. Open Sci., 7, 200556
Hodge J. A. et al., 2016, ApJ, 833, 1
Hopkins P. F., 2015, MNRAS, 450, 53
Hopkins P. F., Quataert E., Murray N., 2011, MNRAS, 417, 950
Hopkins P. F., Narayanan D., Murray N., 2013, MNRAS, 432, 2647
Hopkins P. F., Kereš D., Oñorbe J., Faucher-Giguère C. A., Quataert E., Murray N., Bullock J. S., 2014, MNRAS, 445, 581
Hopkins P. F. et al., 2018a, MNRAS, 477, 1578
Hopkins P. F. et al., 2018b, MNRAS, 480, 800
Hughes D. H. et al., 1998, Nature, 394, 241
James A., Dunne L., Eales S., Edmunds M. G., 2002, MNRAS, 335, 753
Jonsson P., Groves B. A., Cox T. J., 2010, MNRAS, 403, 17
Kereš D., Katz N., Fardal M., Davé R., Weinberg D. H., 2009, MNRAS, 395, 160
Kroupa P., 2002, Science, 295, 82
Krumholz M. R., Gnedin N. Y., 2011, ApJ, 729, 36
Lacey C. G. et al., 2016, MNRAS, 462, 3854
Leitherer C. et al., 1999, ApJS, 123, 3
Liang L., Feldmann R., Faucher-Giguère C.-A., Kereš D., Hopkins P. F., Hayward C. C., Quataert E., Scoville N. Z., 2018, MNRAS, 88, 83
Liang L. et al., 2019, MNRAS, 489, 1397
Lovell C. C., Geach J. E., Davé R., Narayanan D., Li Q., 2021, MNRAS, 502, 772
Ma X., Hopkins P. F., Faucher-Giguère C. A., Zolman N., Muratov A. L., Kereš D., Quataert E., 2016, MNRAS, 456, 2140
Ma X. et al., 2018, MNRAS, 478, 1694
Magnelli B. et al., 2012, A&A, 539, A155
Magnelli B. et al., 2020, ApJ, 892, 66
Marrone D. P. et al., 2018, Nature, 553, 51
McAlpine S. et al., 2016, Astron. Comput., 15, 72
McAlpine S. et al., 2019, MNRAS, 488, 2440
McKinney J., Hayward C. C., Rosenthal L. J., Martinez-Galarza J. R., Pope A., Sajina A., Smith H. A., 2021, ApJ, 921, 55
McKinnon R., Torrey P., Vogelsberger M., Hayward C. C., Marinacci F., 2017, MNRAS, 468, 1505
Miettinen O. et al., 2017, A&A, 606, 1
Miller T. B. et al., 2018, Nature, 556, 469
Muratov A. L., Kereš D., Faucher-Giguère C. A., Hopkins P. F., Quataert E., Murray N., 2015, MNRAS, 454, 2691
Narayanan D. et al., 2010, MNRAS, 407, 1701
Narayanan D. et al., 2015, Nature, 525, 496
Narayanan D. et al., 2021, ApJS, 252, 12
Oesch P. A., Bouwens R. J., Illingworth G. D., Labbé I., Stefanon M., 2018, ApJ, 855, 105
Pandya V. et al., 2021, MNRAS, 508, 2979
Parsotan T., Cochrane R. K., Hayward C. C., Anglés-Alcázar D., Feldmann R., Faucher-Giguère C. A., Wellons S., Hopkins P. F., 2021, MNRAS, 501, 1591
Pillepich A. et al., 2018, MNRAS, 475, 648
Popping G. et al., 2022, MNRAS, 510, 3321
Rowlands K., Gomez H. L., Dunne L., Aragón-Salamanca A., Dye S., Maddox S., da Cunha E., van der Werf P., 2014, MNRAS, 441, 1040
Rupke D. S. N., 2018, Galaxies, 6, 138
Rybak M., McKean J. P., Vegetti S., Andreani P., White S. D., 2015a, MNRAS, 451, L40
Rybak M., Vegetti S., McKean J. P., Andreani P., White S. D., 2015b, MNRAS, 453, L26
Rybak M., Hodge J. A., Vegetti S., van der Werf P., Andreani P., Graziani L., McKean J. P., 2020, MNRAS, 494, 5542
Safarzadeh M., Hayward C. C., Ferguson H. C., 2017, ApJ, 840, 15
Schaller M. et al., 2015, MNRAS, 451, 1247
Schaye J. et al., 2015, MNRAS, 446, 521
Simpson J. M. et al., 2014, ApJ, 788, 125
Smail I., Ivison R. J., Blain A. W., 1997, ApJ, 490, L5
Smail I. et al., 2021, MNRAS, 502, 3426
Somerville R. S., Davé R., 2015, ARA&A, 53, 51
Somerville R. S., Gilmore R. C., Primack J. R., Domínguez A., 2012, MNRAS, 423, 1992
Sparre M., Hayward C. C., Feldmann R., Faucher-Giguère C. A., Muratov A. L., Kereš D., Hopkins P. F., 2017, MNRAS, 466, 88
Springel V. et al., 2005, Nature, 435, 629
Stach S. M. et al., 2018, ApJ, 860, 161
Stach S. M. et al., 2019, MNRAS, 487, 4648
Stach S. M. et al., 2021, MNRAS, 504, 172
Stefanon M., Bouwens R. J., Labbé I., Illingworth G. D., Gonzalez V., Oesch P. A., 2021, ApJ, 922, 29
Steinacker J., Baes M., Gordon K., 2013, ARA&A, 51, 63
Swinbank A. M. et al., 2014, MNRAS, 438, 1267
Tacchella S. et al., 2022, ApJ, 927, 170
Tadaki K.-i. et al., 2017, ApJL, 841, L25
Tielens A. G. G. M., McKee C. F., Seab C. G., Hollenbach D. J., 1994, ApJ, 431, 321
Trayford J. W., Schaye J., 2019, MNRAS, 485, 5715
Trayford J. W. et al., 2015, MNRAS, 452, 2879
Trayford J. W. et al., 2017, MNRAS, 470, 771
Van der Vlugt D. et al., 2021, ApJ, 907, 5
van de Voort F., Quataert E., Hopkins P. F., Kereš D., Faucher-Giguére C. A., 2015, MNRAS, 447, 140
Villaescusa-Navarro F. et al., 2021, ApJ, 915, 71
Villaescusa-Navarro F. et al., 2022, preprint (arXiv:2201.01300)
Vogelsberger M. et al., 2014, MNRAS, 444, 1518
Wang L., Pearson W. J., Cowley W., Trayford J. W., Béthermin M., Gruppioni C., Hurley P., Michałowski M. J., 2019, A&A, 624, 1
Weinberger R. et al., 2017, MNRAS, 465, 3291
Weingartner J. C., Draine B. T., 2001, ApJ, 548, 296
Wellons S. et al., 2022, MNRAS, preprint (arXiv:2203.06201)
Wilkinson A. et al., 2017, MNRAS, 464, 1380
Zavala J. A. et al., 2021, ApJ, 909, 165
Zoldan A., De Lucia G., Xie L., Fontanot F., Hirschmann M., 2019, MNRAS, 487, 5649
Zubko V., Dwek E., Arendt R. G., 2004, ApJS, 152, 211

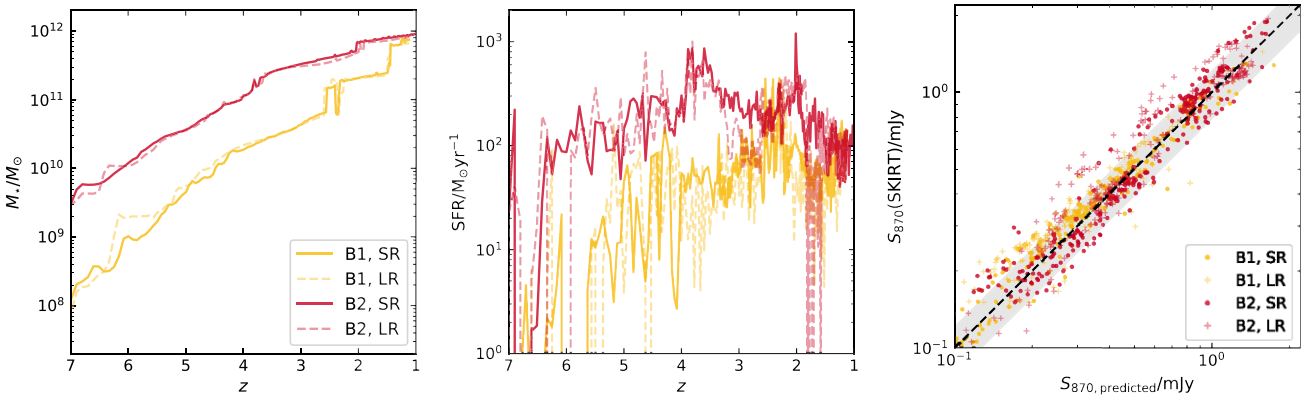

Figure A1. Convergence tests run on haloes B1 and B2. The solid lines show the evolution of stellar mass (left) and instantaneous star formation rate (center) for haloes B1 (yellow) and B2 (red), simulated at our SR. The dashed lines show the evolution of the same quantities for LR simulations of the same haloes. The simulations appear converged at the lower resolution, which is used for the most massive haloes in our sample, C1 and C2. The right-hand panel shows the SKIRT-predicted observed-frame 870 μm flux densities versus our predicted values from the relation derived in Section 3.1 for both the standard- and low-resolution simulations of B1 and B2.

APPENDIX A: RESOLUTION TESTS

We perform convergence tests on the FIRE simulations using haloes B1 and B2. We re-run the zoom-in simulations at LR, to complement the SR simulations used in this work. We find excellent convergence of key properties, including stellar mass and star formation rate (see Fig. A1). We also re-run the radiative transfer on the LR simulations and find no substantive differences in the relationships between sub-millimetre flux density and dust mass or SFR. In the right-hand panel of Fig. A1, we plot SKIRT-predicted observed-frame 870 μm flux densities for the SR and LR runs versus the values predicted from our fit to the SR haloes, presented in Section 3.1. The consistency between SKIRT fluxes derived from the SR and LR runs indicates that the lowest resolution used in this paper (LR) is sufficient for our purposes.

APPENDIX B: CONVERGENCE TESTS WITH RADIATIVE TRANSFER

We perform convergence tests on the parameters used in the radiative transfer. In Fig. B1, we show the SKIRT-predicted SED for halo A1 at $z = 3$, for different SKIRT- parameter choices. We re-run the radiative transfer using 5×10^6 photon packages (compared to the fiducial 1×10^6), maximum fraction of the dust mass per cell 5×10^{-7} (compared to the fiducial 1×10^{-6}), minimum dust grid level 4 (compared to the fiducial 3), and maximum dust grid level 21 (compared to the fiducial 20). The output SED is converged with respect to all these parameters, at all wavelengths.

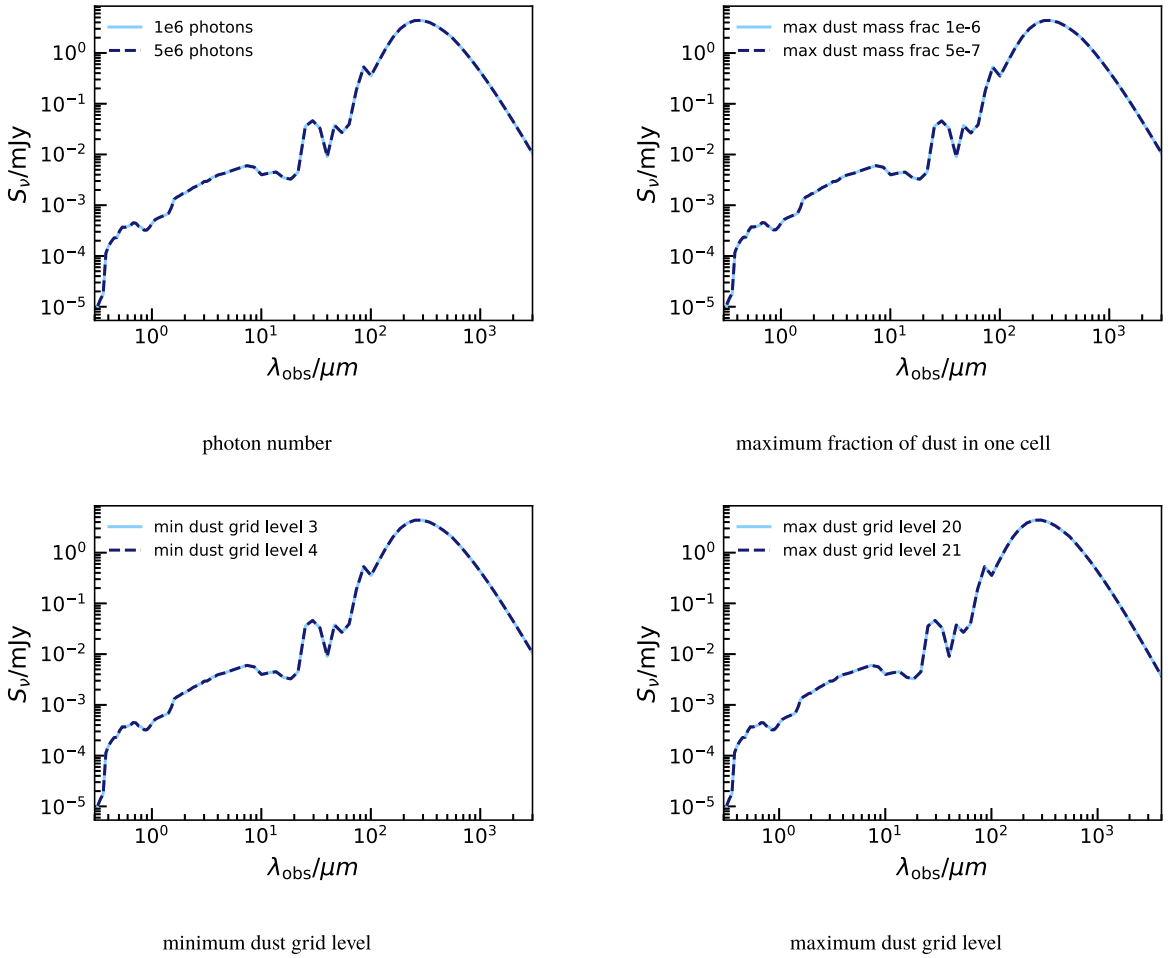

Figure B1. Convergence tests performed on a single halo (A1 at $z = 3$) with SKIRT. The output SED is converged with respect to number of photon packages, maximum fraction of dust in one cell, minimum and maximum dust grid level.

This paper has been typeset from a TEX/LATEX file prepared by the author.